ADVANCED ELECTRONIC MATERIALS Open Access
www.advelectronicmat.de

Microstructural Underpinnings of Giant Intrinsic Exchange Bias in Epitaxial $NiCo_2O_4$ Thin Films

Detian Yang, Arjun Subedi, Chao Liu, Haile Ambaye, Valeria Lauter, Peter A. Dowben, Yaohua Liu, and Xiaoshan Xu**

Understanding intrinsic exchange bias in nominally single-component ferromagnetic or ferrimagnetic materials is crucial for simplifying related device architectures. However, the mechanisms behind this phenomenon and its tunability remain elusive, which hinders the efforts to achieve unidirectional magnetization for widespread applications. Inspired by the high tunability of ferrimagnetic inverse spinel $NiCo_2O_4$, the origin of intrinsic exchange bias in $NiCo_2O_4$ (111) films deposited on Al_2O_3 (0001) substrates are investigated. The comprehensive characterizations, including electron diffraction, X-ray reflectometry and spectroscopy, and polarized neutron reflectometry, reveal that intrinsic exchange bias in $NiCo_2O_4$ (111)/Al_2O_3 (0001) arises from a reconstructed antiferromagnetic rock-salt $Ni_xCo_{1-x}O$ layer at the interface between the film and the substrate due to a significant structural mismatch. Remarkably, by engineering the interfacial structure under optimal growth conditions, it can achieve exchange bias larger than coercivity, leading to unidirectional magnetization. Such giant intrinsic exchange bias can be utilized for realistic device applications. This work establishes a new material platform based on $NiCo_2O_4$, an emergent spintronics material, to study tunable interfacial magnetic and spintronic properties.

1. Introduction

Exchange bias[1,2] refers to the shift of the coercive field of a ferromagnet or ferrimagnet (FM), which is caused by the exchange interaction at the interface between the FM and an antiferromagnet (AFM). This phenomenon is crucial for stabilizing unidirectional magnetization in FM, which has significant applications in magnetic sensors, magnetic recording, and other spintronic devices.[3–5] Interestingly, exchange bias can also occur in systems without a nominal AFM component, a phenomenon known as intrinsic exchange bias,[6–8] which holds promises for simplified device designs.

Intrinsic exchange bias often arises from a "hidden" AFM component formed at the interface between an FM and a non-magnetic material. Achieving optimal intrinsic exchange bias for device applications requires fine-tuning this "hidden" layer. While intrinsic exchange bias has been observed in various interfaces such as $LaNiO_3/LaMnO_3$ superlattices,[9] $La_{2/3}Sr_{1/3}MnO_3/LaSrAlO_4$,[10] $SrRuO_3/LaAlO_3$,[11] Fe/MgO[12] and $La_{0.67}Sr_{0.33}MnO_{3-\delta}/SrTiO_3$,[13] comprehensive studies on its tunability remain scarce. Notably, there have been no reports of achieving unidirectional magnetization through intrinsic exchange bias.

Here we focus on intrinsic exchange bias based on an emergent spintronic material $NiCo_2O_4$ (NCO). NCO is an inverse spinel material with high conductivity (≈1 mΩ cm) and ferrimagnetic order below T_C = 420 K.[14] NCO exhibits large magnetic anisotropy (≈0.7 MJ m^{-3}),[15] strong magnetization (≈2 μ_B f.u.$^{-1}$), and high spin polarization. These properties make it promising for spintronic devices, including tunneling magnetoresistance-based spin valves.[16] Our hypothesis is that for NCO (111)/Al_2O_3 (0001) epitaxial films, the mismatch between the inverse spinel structure of NCO and the corundum structure of Al_2O_3 promotes interfacial reconstruction, potentially forming an AFM layer that can lead to intrinsic exchange bias. Similar behavior has been observed in $CoFe_2O_4$ (111)/Al_2O_3 (0001) thin films.[6] Importantly, epitaxial NCO thin films are highly tunable through growth conditions due to their metastability,[17–27] allowing us to optimize the intrinsic exchange bias.

In this work, we demonstrate a giant intrinsic exchange bias in NCO/Al_2O_3 (0001) thin films, which surpass the coercive field

D. Yang, A. Subedi, P. A. Dowben, X. Xu
Department of Physics and Astronomy and the Nebraska Center for Materials and Nanoscience
University of Nebraska-Lincoln
855 N16th St, Lincoln, NE 68588, USA
E-mail: xiaoshan.xu@unl.edu
C. Liu
Department of Materials Science and Engineering
National University of Singapore
Singapore 117575, Singapore
H. Ambaye, V. Lauter
Neutron Scattering Division
Oak Ridge National Laboratory
Oak Ridge, TN 37830, USA
Y. Liu
Second Target Station
Oak Ridge National Laboratory
Oak Ridge, TN 37830, USA
E-mail: liuyh@ornl.gov
The ORCID identification number(s) for the author(s) of this article can be found under https://doi.org/10.1002/aelm.202400149

DOI: 10.1002/aelm.202400149

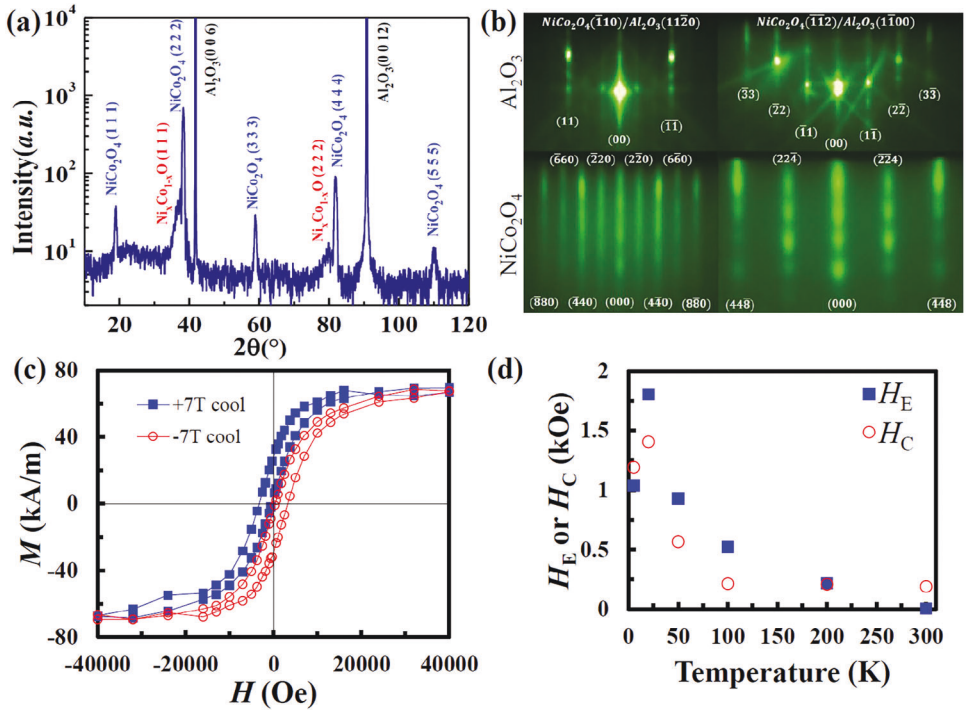

Figure 1. XRD, RHEED, and magnetometry characterization of NCO films grown in 5 mTorr O_2. a) θ–2θ scan of a 15 nm film. b) RHEED patterns of Al_2O_3 and NCO along two perpendicular in-plane directions NCO (−1 1 0) and (−1 −1 2) of the sample in (a). c) Intrinsic exchange bias in a 10 nm film measured at 20 K after cooling in ±70 kOe fields: d) Temperature dependence of exchange bias H_E and coercivity H_C of the film in (c).

and stabilize unidirectional magnetization. To understand the underpinning mechanisms, were conducted thorough characterizations, including electron diffraction, x-ray reflectometry and spectroscopy, and polarized neutron reflectometry. We show that the intrinsic exchange bias originates from a reconstructed rock-salt $Ni_xCo_{1-x}O$ layer at the interface, which exhibits minimal magnetization, a hallmark of robust AFM-supporting exchange bias. Additionally, we found that the thickness of the interfacial layer and its interfacial exchange coupling are sensitive to the sample preparation conditions, allowing for significant tunability of the intrinsic exchange bias.

2. Large Exchange Bias and Unidirectional Magnetization

Figure 1a shows the specular θ–2θ scan of a 15 nm NCO film grown on Al_2O_3 (0001) substrates. Besides the NCO (111) peaks, additional peaks labeled as $Ni_xCo_{1-x}O$ also appear and match well with a rock-salt structure similar to that of CoO and NiO, which indicates the film's complex structural composition and will be discussed later. The diffraction pattern supports the epitaxial growth of the NCO (111) layer. Furthermore, the RHEED pattern in Figure 1b shows the in-plane epitaxial relationship of NCO (−1 1 0) || Al_2O_3 (1 1 −2 0) and confirms the face-centered-cubic structure[28] for which the diffraction peaks are only observed for all-odd and all-even indices.

Figure 1c displays hysteresis loops of NCO measured at 20 K in an in-plane magnetic field after cooling in ± 70 kOe fields, respectively. The coercive field H_C is calculated as half of the separation between the intercepts of the hysteresis loop with the horizontal axis, resulting in a value of 1.4 kOe, which is in agreement with previous work.[29] The exchange bias H_E was calculated as half of the horizontal shift between the two hysteresis loops. Notably, H_E exceeds H_C in Figure 1c, resulting in unidirectional magnetization, a desirable attribute for device applications. Moreover, as shown in Figure 1d, H_E is consistently above H_C except at the lowest temperature (5 K), and at temperatures close to 300 K where H_E vanishes.

3. Comprehensive Characterizations of the Interfacial Layer

The observation of exchange bias in the NCO (111)/Al_2O_3 (0001) films suggests the existence of an interfacial AFM layer, similar to that observed in $CoFe_2O_4$ (111)/Al_2O_3 (0001).[6] Below, we show comprehensive characterizations of this interfacial layer, focusing on its structure, magnetism, and stoichiometry.

3.1. Interfacial "Dead" Layer of Zero Magnetization

An interfacial magnetic "dead" layer in NCO can be inferred from the thickness dependence of the total magnetic moment. As shown in **Figure** 2a, the total moment of NCO films of the same area follows a linear relationship with the film thickness *t*. Interestingly, the extrapolation of the relationship has a finite intercept (3 ± 1 nm) with the horizontal axis, indicating an interfacial layer $t_I = 3 \pm 1$ nm with negligible magnetization.

The "hidden" zero-magnetization interfacial layer also aligns with the thickness dependence of H_E in Figure 2b. Since exchange bias H_E is determined by the competition between the

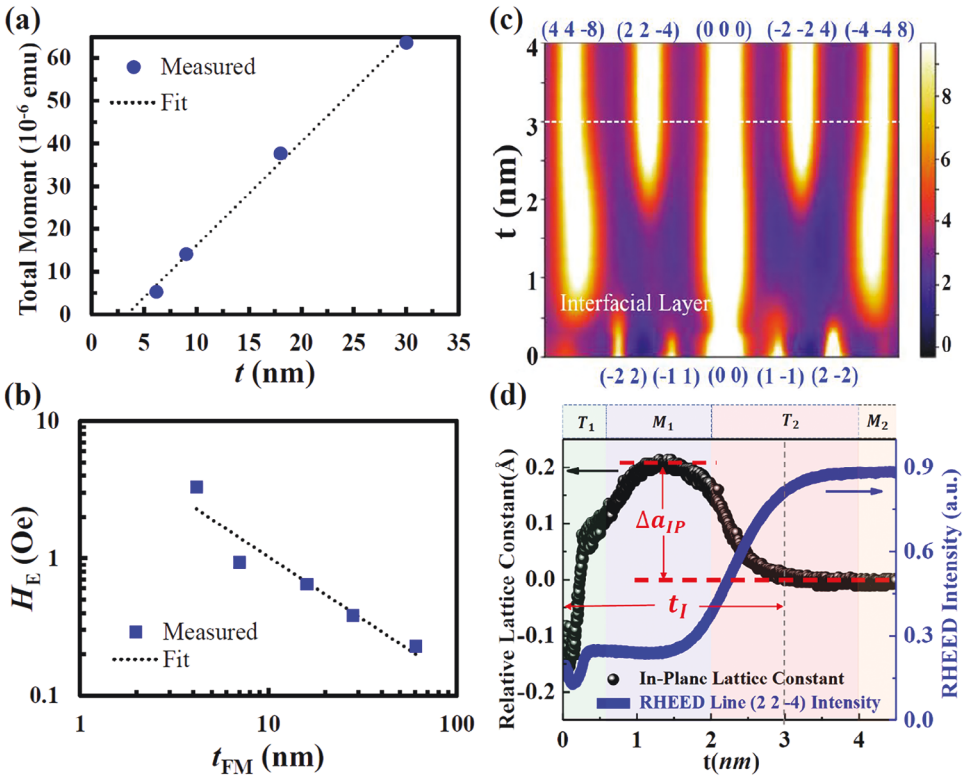

Figure 2. Evidence of an interfacial layer in films grown in 5 mTorr O_2. a) Thickness dependence of saturation moments M_S and the best fit. b) Thickness dependence of exchange bias H_E measured at 50 K with +40 kOe cooling field and the best fit. $t_{FM} = t - t_I$ is the FM layer thickness, where t and t_I are the thickness of the film and the interfacial layer, respectively. c) Typical thickness-resolved RHEED patterns along the in-plane direction [−1 1 0] of NCO; the dashed line marks the boundary of interfacial layers defined in (d). d) Thickness dependence of relative in-plane lattice constant (circles) and (2 2 −4) RHEED line intensity (thick curve) extracted from (c).

AFM/FM interfacial exchange energy and the magnetostatic potential energy of the FM layer, it is expected to decrease with increasing FM layer thickness. As shown in Figure 2b, the thickness dependence can be fit using a power law $H_E \propto \frac{1}{t_{FM}^{0.9}}$, where $t_{FM} = t - t_I$ is the thickness of the FM layer. We found $t_I = 3 \pm 1$ nm from the best fit, consistent with the finding in Figure 2a.

3.2. Rock Salt Crystal Structure

To reveal the crystal structure of the interfacial layer, we recorded thickness-resolved RHEED patterns in situ along the NCO [−1 1 0] in-plane direction. For each thickness, the intensity of the RHEED image is integrated along the streak direction [vertical direction in Figure 1b]. A thickness-resolved RHEED pattern is then obtained by combing the results of varying film thicknesses, as shown in Figure 2c for a film grown in 5 mTorr O_2. This analysis highlighted an interfacial layer, where the diffraction lines (2 2 −4) and (−2 −2 4) are much weaker, and the spacing between the (4 4 −8) and (−4 −4 8) lines is smaller.

To analyze the interfacial layer quantitatively, we extracted from Figure 2c the relative in-plane lattice constant from the spacing between the (4 4 −8) and (−4 −4 8) lines, compared to the value at the thick limit. We also evaluated the intensity of the ± (2 2 −4) lines relative to that of the (4 4 −8) lines as a function of the film thickness. These results are presented in Figure 2d, which revealed three distinctive sublayers of the interfacial layer: one main sublayer, M1, with a larger lattice constant; a transition layer, T1, between the substrate and M1; and a second transition layer, T_2 between M_1; and the "bulk" spinel NCO layer M_2. To characterize the crystal structure of the interfacial layer, we define 1) the interfacial layer thickness t_I as the sum of the thickness of T_1, M_1, and half T_2. In Figure 2d, we found $t_I = 3 \pm 1$ nm, where the error bar is half of the T_2 thickness; and 2) Δa_{IP} as the in-plane lattice constant difference between the interfacial M_1 layer and the "bulk" M_2 layer.

Similar to that in $CoFe_2O_4$ (111)/Al_2O_3 (0001) studied previously,[6] the in-plane crystal structure of the interfacial layer in NCO (111)/Al_2O_3 (0001) is consistent with that of rock salt CoO and NiO. Rock salt's lattice constant is about half that of spinel, explaining the diminishing ± (2 2 −4) lines. The lattice constants of CoO and NiO are slightly larger than half of the lattice constant of spinel NCO, which is in line with the positive Δa_{IP}. Recall that the θ–2θ XRD in Figure 1a shows weak $Ni_xCo_{1-x}O$ (111) peaks, the out-of-plane crystal structure of the interfacial layer is also consistent with the rock salt structure. Therefore, we conclude that the interfacial layer consists mainly of rock salt $Ni_xCo_{1-x}O$ (111), resulting from the reconstruction of the NCO structure to accommodate the lattice mismatch with that of the Al_2O_3 substrate.

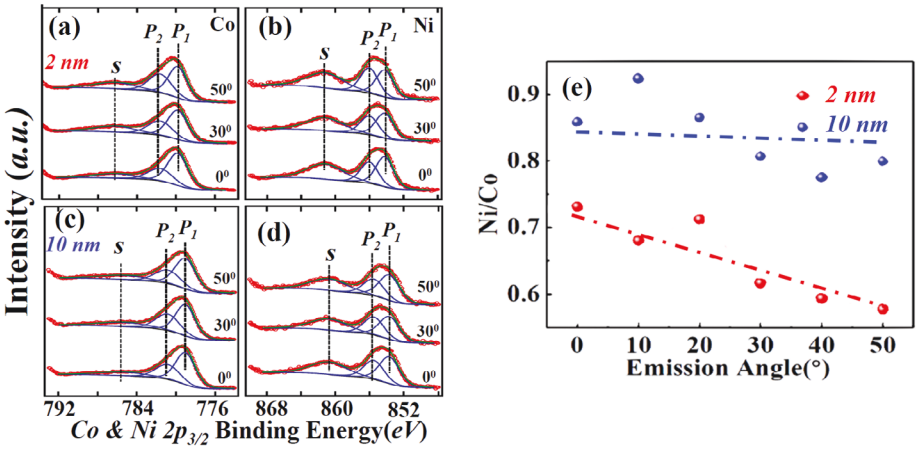

Figure 3. Angle-resolved x-ray photoelectron spectroscopy (ARXPS) of Co and Ni $2p_{3/2}$ core levels in a 2-nm and 10-nm $NiCo_2O_4$ films grown in 5 mTorr O_2 at three emission angles of 0°, 30°, and 50°: a) Co, 2 nm; b) Ni, 2 nm; c) Co, 10 nm; d) Ni, 10 nm. Emission angles are the angles made by photoelectrons relative to the film's surface normal. The Co and Ni core level spectra were fitted by three peaks: P_1, P_2, and S (satellite). e) The Ni to Co intensity ratio in the 2 nm and the 10 nm $NiCo_2O_4$ thin films, after correction with photoemission cross-section. The lines are a guide to the eyes.

3.3. Electronic Structure and Stoichiometry of the Interfacial $Ni_xCo_{1-x}O$

To probe the electronic structure and stoichiometry of the interfacial layer, we carried out angle-resolved x-ray photoelectron spectroscopy (ARXPS) on a 2 nm NCO film, since the electron inelastic mean free path is 2 ±1 nm[30,31] and the interfacial layer thickness $t_I = 3 \pm 1$ nm (see the structural and magnetic characterizations above). A 10 nm NCO film was also studied as a control sample.

Figure 3a–d shows the ARXPS spectra of Co and Ni $2p_{3/2}$ core levels at three photoemission angles, 0°, 30°, and 50°, relative to the films' surface normal. The Co and Ni core levels spectra were decomposed into three components: P_1, P_2, and S (satellite). For the 2 nm film, the intensities of P_1 and P_2 peaks change notably as a function of photoemission angles. Specifically, the ratio of P_1 to P_2 decreases as the angle increases. Since higher angle measurements in ARXPS lead to greater surface sensitivity,[32,33] the observed trend suggests that P1 (P2) peaks correspond to the interior (surface) components. In contrast, in the 10 nm film, P_1/P_2 shows no systematic change on varying angles [Figure 3c,d]. The distinct angle dependencies between the 2-nm and the 10-nm films suggest a strong variation of the film composition in the interfacial layer of the NCO/Al_2O_3 films, which aligns with the complex interfacial structure revealed by RHEED.

Figure 3e shows the two films' stoichiometric ratio between Ni and Co. Although the 2 nm film exhibits a more evident surface-to-interior difference, it still consists of both Co and Ni, according to the substantial Ni/Co ratio. Moreover, the surface (large angle) contains less Ni compared with the interior (small angle), which is corroborated in Section 3.4 by the polarized neutron reflectometry studies below.

3.4. Well-Defined AFM Layer and Pinned Moments

To verify the AFM nature and the multi-layer feature of the interfacial layer, we performed x-ray reflectometry (XRR) and polarized neutron reflectometry (PNR) studies. **Figure** 4a,b shows the XRR data collected at room temperature and the PNR data collected at 20 K, from a 10 nm $NiCo_2O_4$ film grown in 5 mTorr O_2. PNR probes the depth profiles of the nuclear and magnetic scattering length densities (NSLD and MSLD respectively), which correspond to the chemical and in-plane magnetization vector distributions, respectively.[34] To illustrate the magnetic contribution, the spin asymmetry ratio is calculated as $SA = (R^+ - R^-)/(R^+ + R^-)$, where R^+ and R^- are specular reflectivity with neutron spin parallel (+) or antiparallel (–) to the applied field. In the case of zero in-plane magnetization, SA = 0. Figure 4b shows the SA at 20 K in a 40 kOe field after cooling in ± 40 kOe field.

The XRR data and PNR data were co-fitted using the GenX software package;[35,36] the extracted depth profiles are displayed in Figure 4c–e. The minimal model (see Figure S1–S5 and Tables S1 and S2, Supporting Information) to reproduce the experimental results consists of five layers, $Ni_xCo_{1-x}O$ (T_1)/$Ni_yCo_{1-y}O$ (M_1)/$NiCo_2O_4$ (T_2)/$NiCo_2O_4$ (M_2)/$NiCo_2O_4$ (S), as plotted in Figure 4c. Except for the surface layer S, each layer aligns closely with the stratified structure observed in the RHEED analysis, as shown in Figure 2c.

Analyzing the scattering length density profiles for X-ray (XSLD) and neutron nuclear scattering (NSLD) depicted in Figure 2d reveals insightful contrasts. For X-ray scattering, the scattering lengths of elements are proportional to their atomic numbers, which means Ni and Co dominate. Therefore, a smaller X-ray SLD in the T_1 layer, compared with that in the M_1 layer, is likely due to a substantial amount of Ni or Co vacancies. From the M_1 layer and above, the XSLD stays approximately constant, indicating a fixed total concentration of the metal atoms, because Co and Ni have almost the same atomic number. For neutron nuclear scattering, the coherent scattering lengths are 10.3 fm, 2.49 fm, and 5.8 fm for Ni, Co, and O, respectively. This high contrast translates to a better sensitivity to the chemical composition. Indeed, NSLD exhibits more prominent variations across the M_1, T_2, and M_2 layers. Given Ni's much larger scattering length, the Ni concentration is likely higher in the M_1 layer than in the T_2 layer. XPS measurements in Section 3.3, presumably probing the

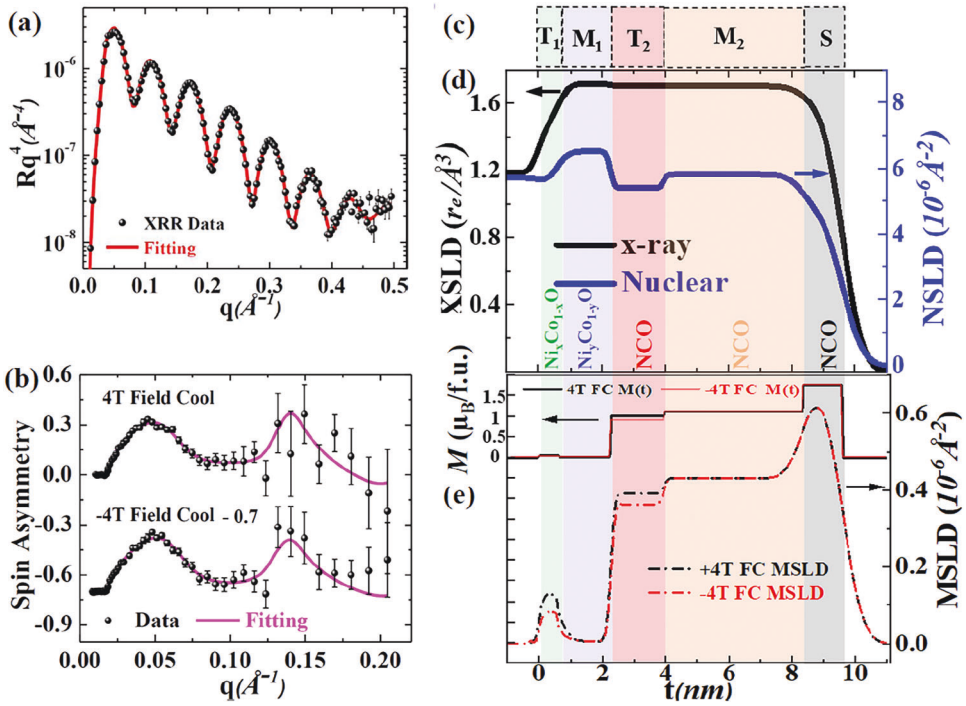

Figure 4. a) Scaled X-ray reflectivity Rq^4 at 300 K (circles) and the best fit (line) as a function of momentum transfer q of a 10 nm $NiCo_2O_4$ thin film grown in 5 mTorr O_2. b) Spin asymmetry (circles) and the best fit (lines) extracted from polarized neutron reflectometry measured in 40 kOe field at 20 K after cooling down in 40 kOe field and −40 kOe field (shifted by −0.7 for clarity). c) Five-layer model $Ni_xCo_{1-x}O(T_1)/Ni_yCo_{1-y}O(M_1)/NCO(T_2)/NCO(M_2)/NCO(S)$. Depth profiles of X-ray scattering length density (XSLD) and nuclear neutron scattering length density (NSLD) d) and nuclear neutron scattering length density (MSLD) e) derived from both the X-ray and neutron reflectometry. The fitted roughness of the surface layer and transition layers are no larger than 30% of their thicknesses and the roughness of the main layers is no larger than 10% of their thicknesses. $r_e = 2.82$ fm is the classical electron radius. The magnetization in (e) was calculated based on the $NiCo_2O_4$ lattice constant $a_{NCO} = 8.184$Å and the interfacial layer lattice constant $a_I = 4.192$Å from the XRD measurement and RHEED data.

top M_1 layer (interior) and the bottom T_2 layer (surface), corroborate these findings by indicating a decreasing Ni concentration in the 2 nm NCO film from the interior to the surface.

Figure 4e presents the depth profiles of magnetization at 40 kOe with ± 40 kOe cooling fields. In both cases, the M_1 sublayer has zero magnetization, affirming a well-defined AFM $Ni_xCo_{1-x}O$ layer. The T_1 sublayer has a small net moment, most likely due to uncompensated spins and oxygen vacancies in the AFM $Ni_xCo_{1-x}O$. Furthermore, the magnetizations of T_1 and T_2 layers are smaller with the −40 kOe cooling field than with the 40 kOe cooling field, suggesting that some spins in these layers were pinned to the cooling field direction, validating the exchange bias mechanism.

4. Tunable Interface Thickness and Exchange Bias by Growth Oxygen Pressure

The interfacial reconstruction and exchange bias can be effectively tuned by the oxygen pressure in the growth processes. A series of NCO films, each 9 ± 1 nm, were fabricated with oxygen pressures varying from 1 mTorr to 200 mTorr. Thickness-resolved RHEED patterns of the films were recorded; the interfacial layer thickness extracted from these RHEED patterns is plotted relative to oxygen pressure, together with exchange bias H_E measured at 50 K with 40 kOe cooling field, as shown in **Figure** 5a. The interfacial layer thickness monotonically increases as the oxygen pressure P_{O2} decreases. The relationship can be described by $t_1 = t_{10} \ln(P_0/P_{O2})$, where $t_{10} = 0.56$ nm and $P_0 = 901$ mTorr. This trend can be attributed to lower P_{O2} favoring the rock salt structure due to its lower oxygen content than the spinel structure. In contrast, the exchange bias demonstrates a non-monotonic feature, peaking at an oxygen pressure of 5 mTorr.

Figure 5b illustrates the structural models ($0 \le t \le 6$ nm) for three films grown with 1 mTorr, 5 mTorr, and 20 mTorr O_2, derived by co-fitting XRR measured at 300 K and PNR data measured at 20 K in a +40 kOe field after being cooled down in ± 40 kOe fields. These models (see details in Figures S7, S8, Supporting Information) visualize the spin arrangements of all layers at +40 kOe and 20 K after cooling the samples in a +40 kOe field. Figure 5c shows the refined thicknesses of AFM component $Ni_xCo_{1-x}O$ (T_1+M_1) and the transition layer T_2; both decrease as the oxygen pressure increases, consistent with the RHEED data in Figure 5a (see also Figure S9, Supporting Information).

5. Discussion

The non-monotonic dependence of H_E on oxygen pressure shown in Figure 5a suggests competing factors underpinning the exchange bias. The decreased H_E for $P_{O2} > 5$ mTorr can be linked to the narrowing of the interfacial AFM layer. Higher P_{O2} reduces the thickness of the interfacial layer [Figure 5a], and the exchange bias is expected to drop rapidly once the thickness of the AFM

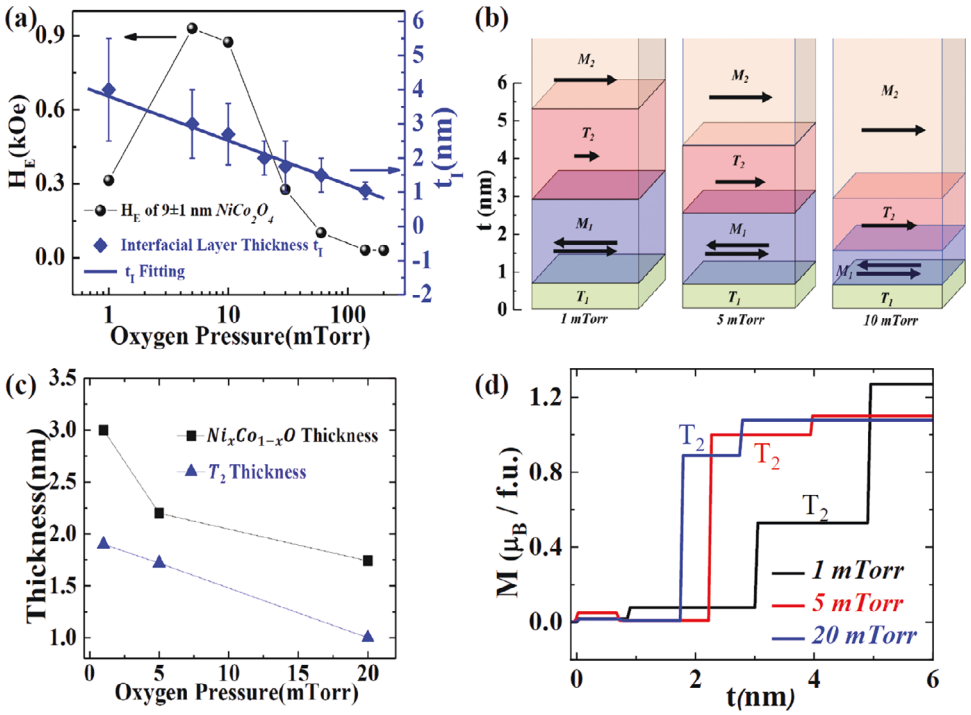

Figure 5. a) Growth O_2-pressure dependence of exchange bias H_E (black circles) and interfacial layer thickness t_I (diamonds) and the best fit for $t = 9 \pm 1$ nm $NiCo_2O_4$ films. H_E was measured at 50K with a cooling field of 40 kOe. b) Structural models around the interfacial layers for three films grown with 1 mTorr, 5 mTorr, and 20 mTorr O_2 derived by co-fitting the XRR and PNR data. The in-plane magnetization in +40 kOe field at 20 K is illustrated by the arrows, and the pair of opposite arrows in M_1 and T_1 areas indicates the antiferromagnetic spin arrangements. c) Growth O_2-pressure dependence of total $Ni_xCo_{1-x}O$ layer (T_1+M_1) thickness and the T_2 thickness according to (b). d) Depth profiles of the magnetizations at 20 K in a 40 kOe field after cooling in a +40 kOe field for the three films illustrated in (b). The T_2 transition layers are labeled explicitly to emphasize the relatively smaller magnetization of T_2 for the film grown in 1 mTorr O_2.

layer falls below a critical thickness.[37] Here the critical thickness appears to be ≈1.9 nm, i.e., the thickness of the $Ni_xCo_{1-x}O$ layers (T_1 + M_1) at P_{O2} = 10 mTorr, close to the critical thickness (1.6 nm) of CoO observed in the Fe_3O_4/CoO heterostructure.[38] Interestingly, unlike Fe_3O_4/CoO,[39] the blocking temperature (≈300 K) in the NCO film samples grown with 5 mTorr O_2 does not decrease, although the $Ni_xCo_{1-x}O$ AFM layer is only 2.2 nm thick.

The lower H_E for P_{O2} < 5 mTorr suggests a diminished exchange coupling between the AFM and the FM layer. When the AFM layer is thicker than the critical thickness, it can be considered rigid except for some twists at the interface.[40] In this case, the exchange coupling at the interface is vital to the exchange bias. The T_2 transition layer is crucial in determining the coupling since it corresponds to the structural transition from the AFM $Ni_xCo_{1-x}O$ layers to the FM $NiCo_2O_4$ M_2 layer. As shown in Figure 5d, for the films grown in P_{O2} = 5 and 20 mTorr, the magnetization of the T_2 transition layer is close to that of the M_2 layer, suggesting a well-ordered T_2 transition layer and a well-defined AFM/FM interface. In contrast, for the film grown in P_{O2} = 1 mTorr, the magnetization of the T_2 transition layer is halfway between the M_1 and the M_2 layers, suggesting a T_2 transition layer with significant disorders and a smeared interface, which will reduce the interfacial coupling. Consider the rigid rotation model, exchange bias $H_E \propto \frac{\Delta\sigma}{M_{T_2}t_{T_2}+M_{M_2}t_{M_2}}$,[41] where M_{T_2} (M_{M_2}) and t_{T_2} (t_{M_2}) are the magnetization and thickness of the T_2 (M_2) layer, respectively. Using the magnetization profile in Figure 5d, we calculated $M_{T_2}t_{T_2} + M_{M_2}t_{M_2}$ for the 10 nm films grown in P_{O2} = 1 and 5 mTorr and found 7.5 and 7.6 μ_B nm f.u.$^{-1}$, respectively, which are virtually the same. Since the denominator $M_{T_2}t_{T_2} + M_{M_2}t_{M_2}$ in the exchange bias formula is only moderately changed, the reduction of the interfacial exchange energy $\Delta\sigma$ would effectively decrease the measured exchange bias value. Moreover, the M_1 layer in the 1-mTorr film displays a small but discernible net magnetization without exhibiting higher NSLD than the M_2 layer, contrasting with findings for 5-mTorr and 20-mTorr samples. This suggests inferior AFM layer quality at lower oxygen pressures. Therefore, reduced H_E for P_{O2} < 5 mTorr can be attributed to microstructural imperfections in the M_1 and T_2 interface layers.

6. Conclusion

We demonstrated beyond-coercivity intrinsic exchange bias originated from interfacial reconstruction in $NiCo_2O_4$ (111)/Al_2O_3 (0001) films. The "hidden" antiferromagnetic layer is identified as the rock-salt $Ni_xCo_{1-x}O$ at the interface, supported by comprehensive analysis including RHEED, magnetometry, XPS, XRR, and PNR. The ability to control interfacial reconstruction and intrinsic exchange bias using growth oxygen pressure underscores the application potential of this approach. This work establishes new material platforms to study novel interfacial structural and

magnetic states for magnetic storage and spintronics. It also highlights the powerful interface engineering strategy in manipulating material functionalities.

7. Experimental Section

Sample Preparation: The (111)-oriented $NiCo_2O_4$ thin films were grown on Al_2O_3 (0001) substrates by pulsed laser deposition (PLD) with oxygen pressures from 1 to 200 mTorr at 300 °C with a KrF excimer laser of wavelength 248 nm, pulse energy 120 ± 10 mJ, and repetition rate 4 Hz. The growth processes were monitored by a reflection high energy electron diffraction (RHEED) system.

X-Ray Diffraction and Magnetometry: Specular $\theta-2\theta$ X-ray diffraction (XRD) and X-ray reflectometry (XRR) were conducted by a Rigaku SmartLab X-ray diffractometer (wavelength 1.5406 Å); the film thicknesses were extracted from the XRR data. The in-plane crystal structure was studied by analyzing the RHEED patterns. The magnetic hysteresis loops were measured between 5 and 300 K in a superconducting quantum interference device (SQUID) system after being cooled down from 320 K in ± 40 kOe or ± 70 kOe fields.

X-Ray Photoemission Spectroscopy: X-ray photoemission spectra (XPS) were acquired using a VG100AX hemispherical analyzer and a SPECSX-ray Mg Kα anode (1253.6 eV) source. All the XPS measurements were carried out at room temperature in an ultra-high vacuum chamber with a base pressure lower than 3×10^{-9} Torr.

Polarized Neutron Reflectometry: Polarized neutron reflectometry (PNR) experiments were performed on the Magnetism Reflectometer at the Spallation Neutron Source at Oak Ridge National Laboratory[34] using neutron beams with wavelengths λ in a band of 2–8 Å and a polarization of 98.5–99% using a 5 T cryomagnet.

Supporting Information

Supporting Information is available from the Wiley Online Library or from the author.

Acknowledgements

The authors acknowledge the primary support from the National Science Foundation (NSF) through EPSCoR RII Track-1: Emergent Quantum Materials and Technologies (EQUATE), Award No. OIA-2044049. The research was performed in part in the Nebraska Nanoscale Facility: National Nanotechnology Coordinated Infrastructure and the Nebraska Center for Materials and Nanoscience, which are supported by the NSF under Grant No. ECCS-2025298, and the Nebraska Research Initiative. A portion of this research used resources at the Spallation Neutron Source, a DOE Office of Science User Facility operated by the Oak Ridge National Laboratory. D. Y. is currently at Shanghai University.

Conflict of Interest

The authors declare no conflict of interest.

Author Contributions

X.X., Y.L., and D.Y. performed conceptualization. X.X., D.Y., and A.S. performed the methodology. D.Y., A.S., C. L., H.A., and V.L. performed formal analysis. D.Y., A.S., Y.L., H.A., and V.L. performed the investigation. D.Y. and A. S. performed writing – original draft preparation. X.X., Y.L., P.D., C.L., H.A., and V.L. performed writing – review & editing. X.X. and Y.L. performed supervision. X.X. and P.D. performed funding acquisition. All authors have read and agreed to the published version of the manuscript.

Data Availability Statement

The data that support the findings of this study are available in the supplementary material of this article.

Keywords

intrinsic exchange bias, nickel cobaltate, oxide thin films, polarization neutron reflection, X-ray photoemission spectroscopy

Received: February 26, 2024
Revised: June 7, 2024
Published online: November 15, 2024

[1] J. Nogués, J. Sort, V. Langlais, V. Skumryev, S. Suriñach, J. S. Muñoz, M. D. Baró, *Phys Rep.* **2005**, *422*, 65.
[2] W. Zhang, K. M. Krishnan, *Materials Science and Engineering R: Reports* **2016**, *105*, 1.
[3] S. S. P. Parkin, K. P. Roche, M. G. Samant, P. M. Rice, R. B. Beyers, R. E. Scheuerlein, E. J. O'Sullivan, S. L. Brown, J. Bucchigano, D. W. Abraham, Y. Lu, M. Rooks, P. L. Trouilloud, R. A. Wanner, W. J. Gallagher, *J. Appl. Phys.* **1999**, *85*, 5828.
[4] J. C. S. Kools, *IEEE transactions on magnetics* **1996**, *32*, 3165.
[5] S. Gider, B.-U. Runge, A. C. Marley, S. S. P. Parkin, *Science (1979)* **1998**, *281*, 797.
[6] D. Yang, Y. Yun, A. Subedi, N. E. Rogers, D. M. Cornelison, P. A. Dowben, X. Xu, *Phys. Rev. B* **2021**, *103*, 224405.
[7] Z. Kong, C. J. Kaminsky, C. K. Groschner, R. A. Murphy, Y. Yu, S. Husremović, L. S. Xie, M. P. Erodici, R. S. Kim, J. Yano, D. K. Bediako, *J. Am. Chem. Soc.* **2023**, *145*, 20041.
[8] S. Karmakar, S. Taran, E. Bose, B. K. Chaudhuri, C. P. Sun, C. L. Huang, H. D. Yang, *Phys. Rev. B Condens Matter Mater. Phys.* **2008**, *77*, 144409.
[9] M. Gibert, P. Zubko, R. Scherwitzl, J. Íñiguez, J. M. Triscone, *Nat. Mater.* **2012**, *11*, 195.
[10] B. Cui, C. Song, G. Y. Wang, H. J. Mao, F. Zeng, F. Pan, *Sci Rep.* **2013**, *3*, 2542.
[11] C. Sow, A. K. Pramanik, P. S. Anil Kumar, *J. Appl. Phys.* **2014**, *116*, 194310.
[12] Y. Fan, K. J. Smith, G. Lüpke, A. T. Hanbicki, R. Goswami, C. H. Li, H. B. Zhao, B. T. Jonker, *Nat. Nanotechnol.* **2013**, *8*, 438.
[13] D. Schumacher, A. Steffen, J. Voigt, J. Schubert, T. Brückel, H. Ambaye, V. Lauter, *Phys. Rev. B* **2013**, *88*, 144427.
[14] X. Xu, C. Mellinger, Z. G. Cheng, X. Chen, X. Hong, *J. Appl. Phys.* **2022**, *132*, 020901.
[15] C. Mellinger, J. Waybright, X. Zhang, C. Schmidt, X. Xu, *Phys. Rev. B* **2020**, *101*, 14413.
[16] Y. Shen, D. Kan, I.-C. Lin, M.-W. Chu, I. Suzuki, Y. Shimakawa, *Appl. Phys. Lett.* **2020**, *117*, 42408.
[17] X. Chen, X. Zhang, M. Han, L. Zhang, Y. Zhu, X. Xu, X. Hong, *Adv. Mater.* **2019**, *31*, 1805260.
[18] Y. Bitla, Y.-Y. Chin, J.-C. Lin, C. N. Van, R. Liu, Y. Zhu, H.-J. Liu, Q. Zhan, H.-J. Lin, C.-T. Chen, Y.-H. Chu, Q. He, *Sci. Rep.* **2015**, *5*, 15201.
[19] P. F. Ndione, Y. Shi, V. Stevanovic, S. Lany, A. Zakutayev, P. A. Parilla, J. D. Perkins, J. J. Berry, D. S. Ginley, M. F. Toney, *Adv. Funct. Mater.* **2014**, *24*, 610.
[20] P. Silwal, L. Miao, I. Stern, X. Zhou, J. Hu, D. Ho Kim, *Appl. Phys. Lett.* **2012**, *100*, 032102.
[21] P. Silwal, L. Miao, J. Hu, L. Spinu, D. Ho Kim, D. Talbayev, *J. Appl. Phys.* **2013**, *114*, 103704.
[22] P. Silwal, C. La-O-Vorakiat, E. E. M. Chia, D. H. Kim, D. Talbayev, *AIP Adv.* **2013**, *3*, 092116.

[23] K. Dileep, B. Loukya, P. Silwal, A. Gupta, R. Datta, *J. Phys. D Appl. Phys.* **2014**, *47*, 405001.
[24] P. Li, C. Xia, J. Li, Z. Zhu, Y. Wen, Q. Zhang, J. Zhang, Y. Peng, H. N. Alshareef, X. Zhang, *ACS Nano* **2017**, *11*, 5011.
[25] I. Suzuki, D. Kan, M. Kitamura, Y. Shen, K. Horiba, Y. Shimakawa, *J. Appl. Phys.* **2020**, *127*, 203903.
[26] Y. Shen, D. Kan, Z. Tan, Y. Wakabayashi, Y. Shimakawa, *Phys. Rev. B* **2020**, *101*, 094412.
[27] M. Xue, X. Chen, S. Ding, Z. Liang, Y. Peng, X. Li, L. Zha, W. Yang, J. Han, S. Liu, H. Du, C. Wang, J. Yang, *ACS Appl. Electron. Mater.* **2020**, *2*, 3964.
[28] K. E. Sickafus, J. M. Wills, N. W. Grimes, *J. Am. Ceram. Soc.* **1999**, *82*, 3279.
[29] C. Zhen, X. Zhang, W. Wei, W. Guo, A. Pant, X. Xu, J. Shen, L. Ma, D. Hou, *J. Phys. D. Appl. Phys.* **2018**, *51*, 145308.
[30] S. Tanuma, C. J. Powell, D. R. Penn, *Surf. Interface Anal.* **2011**, *43*, 689.
[31] W. S. M. Werner, C. Tomastik, T. Cabela, G. Richter, H. Störi, *Surf Sci.* **2000**, *470*, L123.
[32] A. Subedi, D. Yang, Y. Yun, X. Xu, P. A. Dowben, *J. Vac. Sci. Technol. A* **2022**, *40*.
[33] P. A., M. A. Dowben, *Surface Segregation Phenomena*, 1st eds., CRC Press, Boca Raton, FL, **1990**.
[34] V. Lauter, H. Ambaye, R. Goyette, W. T. Hal Lee, A. Parizzi, *Physica B* **2009**, *404*, 2543.
[35] A. Glavic, M. Björck, *J. Appl. Crystallogr.* **2022**, *55*, 1063.
[36] M. Björck, G. Andersson, *J. Appl. Crystallogr.* **2007**, *40*, 1174.
[37] J. Nogués, I. K. Schuller, *J. Magn. Magn. Mater.* **1999**, *192*, 203.
[38] P. J. Van Der Zaag, A. R. Ball, L. F. Feiner, R. M. Wolf, P. A. A. Van Der Heijden, *J. Appl. Phys.* **1996**, *79*, 5103.
[39] P. J. Van Der Zaag, Y. Ijiri, J. A. Borchers, L. F. Feiner, R. M. Wolf, J. M. Gaines, R. W. Erwin, M. A. Verheijen, *Phys. Rev. Lett.* **2000**, *84*, 6102.
[40] R. L. Stamps, *J. Phys. D Appl. Phys.* **2000**, *33*, R247.
[41] A. E. Berkowitz, K. Takano, *J. Magn. Magn. Mater.* **1999**, *200*, 552.